Topological modes for light propagation inside a 2D photonic square lattice crystal with $p4$ symmetry

M. A. Tun-Carrillo

Posgrado en Ciencias-IICBA, Universidad Autónoma del Estado de Morelos, Av. Universidad No. 1001, 62209, Cuernavaca, Morelos, México; e-mail: marco.tun@uaem.edu.mx Orcid: 0009-0008-4813-5365

J. A. Medina-Vázquez

Centro de Investigación en Materiales Avanzados S.C, Complejo Industrial Chihuahua, Miguel de Cervantes 120, 31136, Chihuahua, México. Orcid: 0000-0001-6012-7933

M. E. Mora-Ramos*

*Centro de Investigación en Ciencias-IICBA, Universidad Autónoma del Estado de Morelos, Av. Universidad No. 1001, 62209, Cuernavaca, Morelos, México, *e-mail: memora@uaem.mx Orcid:0000-0002-6232-9958*

H. A. Gómez-Urrea

Instituto de Ciencias Básicas, Universidad de Medellín, 050026, Medellín, Colombia, Orcid: 0000-0003-0611-2428

I. V. Pérez-Quintana

Facultad de Ingeniería, Universidad Autónoma de Yucatán, Industrias No Contaminantes S/N, Sin Nombre de Col 27, 97302, Mérida, Yucatán, México. Orcid: 0000-0003-2802-4760

Received 12 January 2026; accepted 2 October 2026

We investigate a two-dimensional all-dielectric silicon photonic crystal with a square lattice based on $p4$ space group wallpaper symmetry, demonstrating dual-functional electromagnetic response. By employing group-theoretical symmetry indicators, we characterize the topological phase hierarchy of the lower ten transverse magnetic (TM) bands for two complementary unit cell configurations (UC1 and UC2). The topological non-triviality of UC2 enables the emergence of robust edge and corner modes within the telecommunication window (~ 1.84 THz / 1.6 μm) at the interface with the trivial UC1 phase. Additionally, an accidental p–p–d band degeneracy forming a Dirac-like cone at the Γ point yields a near-zero refractive index (NZRI) regime in the mid-infrared region (~ 1.03 THz / 2.9 μm). We discuss the interplay between time-reversal symmetry-protected degeneracies and the absence of monopolar (s-like) symmetry, which results in directional impedance variations and non-ideal wave-front flattening. These findings highlight the potential of simple square-lattice geometries for integrated topological routing, directional optical sensing, and light manipulation.

Keywords: Higher-order topological modes; photonic crystal; topological edge and corner states; light localization.

DOI: https://doi.org/10.31349/RevMexFis.72.061302

1. Introduction

In modern photonics, efficient control of light propagation is essential for applications in telecommunications, sensors, information processing, and optical computing [1-3]. Traditionally, waveguides have been designed using refractive index contrasts, confining light to specific regions through total internal reflection or periodic structures such as photonic crystals [4]. However, these methods are typically sensitive to manufacturing imperfections, misalignments, and structural disorders, which hinder their robustness and scalability.

In contrast, topological boundaries in photonic systems offer a revolutionary alternative based on the principles of solid-state physics, specifically band topology. These waveguides form at the boundaries between two materials with different topological invariants, allowing the emergence of topologically protected edge modes. Such modes can propagate without dispersion, even in the presence of defects, curvatures, or irregularities, giving them unprecedented robustness against disorder [1,5-7].

The realization of topological boundaries in optical waveguides not only enhances tolerance to structural defects

but also enables the development of more compact, efficient, and robust integrated photonic devices. Notably, the influence of edge and corner states on light propagation exhibits a strong analogy with the behavior of electronic transport in dislocation pathways within graphene structures [7-9].

Modern topological photonics have made incredible advances regarding hexagonal and more exotic cell structures; from a technological perspective squared lattices may be a more feasible way to implement topological wave guides, given the simplicity of it's geometry [6,10,11]. This type of geometry is compatible with standard manufacturing techniques, such as electron lithography or deep etching, facilitating their integration into photonic chips. By breaking certain spatial symmetries-such as rotational symmetries-in a square lattice, it is possible to induce topological phases that support robust edge modes.

Modern material science, in particular the engineering of metamaterials, have made the ideal playground for the study of photonic structures that may present multiple functionalities through the appearance of different phenomena, such as Near Zero Refractive Index (NZI) and topological light propagation [12-14].

In this article, we propose a particular example of a two-dimensional photonic crystal (2DPC) with square lattice geometry based on the $p4$ symmetry (a type characterized by 90° rotations), which allows for the propagation of high-sensitivity corner and border modes, considered topological borders. Photonic properties, such as band structure and transmission, are discussed within the framework of the analysis as well.

2. Design and methodology

The design –perhaps the simplest wallpaper-like– resembles that of a pinwheel that tiles the plane. Both unitary cells correspond to a pattern that clearly presents fourth-order rotational symmetry (90° rotation) around the center, without horizontal, vertical, or diagonal reflection clearly being a $p4$ symmetry [15]. A schematic view of the dielectric structure is displayed in Fig. 1. Simulations are carried out using COMSOL package [16]. The materials of choice are air (white areas) and silicon (orange areas) using $\varepsilon_{Si} = 12.25$. Technologically speaking, this design would be simple and easy to produce using traditional methods of deposition, such as RF sputtering.

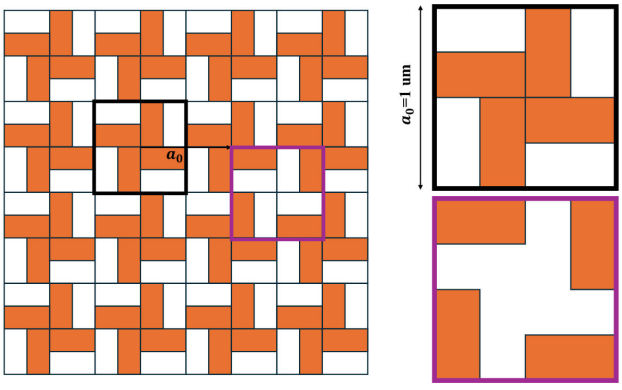


FIGURE 1. On the left we observe the pattern as it tiles the plane. On the right we see the two possible primitive cells that make the pattern, UC1 (Top) and UC2 (Bottom).

In the case of topological mode propagation, we need to identify which unitary cell (UC) is trivial and which one is non-trivial, according to the accepted classification. The topological characterization of a photonic crystal band relies on identifying how its Bloch eigenmodes transform under the crystalline symmetries of the lattice. In what follows, we shall provide a detailed description of the procedure.

The topological characterization of photonic crystal bands under crystalline symmetries is fundamentally rooted in the representation theory of space groups applied to the Maxwell eigen-problem [17]. In a periodic dielectric medium, the electromagnetic modes are described by Bloch functions of the form.

$$\mathbf{E}_{n,\mathbf{k}}(\mathbf{r}) = e^{i\mathbf{k}\cdot\mathbf{r}}\mathbf{u}_{n,\mathbf{k}}(\mathbf{r}), \tag{1}$$

where $\mathbf{u}_{n,\mathbf{k}}(\mathbf{r})$ represents the periodic part of the electric field that satisfies the lattice periodicity condition, $\mathbf{k}$ is the Bloch wave vector defined within the first Brillouin zone, n is the label for the given band, and $\mathbf{r}$ is the position vector in real space.

Inside the band diagram, there are certain points of high symmetry (HSP's) in the Brillouin zone, which define non-trivial point group symmetries. At these high symmetry points (HSPs), the corresponding little group contains point-group operations-such as discrete rotations-that commute with the Maxwell operator, allowing the Bloch modes to be chosen as simultaneous eigen-states of these symmetry operations as well [18]. For a $n-$fold rotational symmetry, the action of the rotation operator $\hat{C}_n$ over the periodic part of the electric field is given as

$$(\hat{C}_n)(\mathbf{r}) = R_n u(R_n^{-1}\mathbf{r}), \tag{2}$$

where R_n is the matrix corresponding to a rotation by an angle of $2\pi/n$ about the symmetry axis. R_n accounts for the transformations of the vector field components under rotation. As mentioned, at the HSP points, the rotation operator and the Maxwell operator must commute. Therefore, the eigenmodes can be chosen to transform according to irreducible representations of the rotation group. To extract the rotation eigenvalues λ in a gauge-invariant manner, we compute the normalized expectation value

$$\lambda = \frac{\langle u \mid \hat{C}_n u\rangle}{\langle u \mid u\rangle}, \tag{3}$$

Here, the operator $< \mid >$ denotes the inner product over the unit cell, defined as

$$< f|g >= \int_{UC} f^*(\mathbf{r}) \bullet g(\mathbf{r}) d\mathbf{r}.$$

The normalization in the denominator ensures that λ is independent of the absolute field amplitude and invariant under global phase transformations $u \to e^{i\phi}u$.

This operation returns a phase factor of the form $e^{2\pi ip/n}$ when the field is an irreducible eigenstate of the symmetry operation. Because the Maxwell operator commutes with $\hat{C}_n$ only at the HSPs, the extraction of these eigenvalues at Γ, X, M, K, provides a symmetry-protected and gauge-independent fingerprint for the transformation properties of the investigated modes [19].

Once the rotation eigenvalues $\lambda_{n,\mathbf{k}}$ have been calculated for each band at each HSP, the next step consists in assembling these local symmetry data into global, gauge-invariant topological quantities known as symmetry-based invariants or symmetry indicators. These invariants capture the obstruction to providing a complete classification of crystalline topological phases within the symmetry class under consideration [17,19].

Let K be the set of all high-symmetry points (HSPs) invariant under a given rotational symmetry C_n. For each $\mathbf{k} \in K$, one can define the integer multiplicities:

$$N_p^{\mathbf{k}}, \quad p \in \{0, 1, \ldots, n-1\}. \tag{4}$$

Here, $N_p^{\mathbf{k}}$ counts the number of bands below the band gap (or within the chosen frequency range) whose rotation eigenvalue equals $\lambda_p = e^{2\pi ip/n}$. These multiplicities define a representation vector in the free Abelian group $\mathbb{Z}^{|K|\times n}$. Further details on this topological classification framework can be found in the work by Vaidya *et al.* [20].

To isolate genuinely topological features, one must therefore construct quantities in which all atomic-limit contributions cancel out. This is naturally achieved by forming differences between representation multiplicities at different high-symmetry points that share the same symmetry or belong to the same little group, leading to robust symmetry-based invariants [21].

The canonical way to define such differences is in the form

$$[\Pi_p^{(n)}] = \Pi_p^{(\Pi)} - \Pi_p^{(\Gamma)}, \tag{5}$$

where Γ denotes the Brillouin zone center and Π denotes another HSP invariant under the same rotation invariance, such as M in lattices with C_4 symmetry. For any elementary band representation induced from localized Wannier functions, the number of states transforming with a given angular momentum p is identical at all HSPs connected by symmetry. Consequently, atomic bands contribute equally to $N_p^{(\Gamma)}$ and $N_p^{(\Pi)}$, causing their difference to vanish identically [17]. Therefore, a nonzero value of $[\Pi_p^{(n)}]$ signals a genuine topological obstruction.

Now, the topological characterization of the photonic modes can be formulated in terms of the geometric phase accumulated under crystalline rotations at high-symmetry points in the Brillouin zone [20,22]. This is defined by the following equation:

$$\chi^{(4)} = ([X_1^{(2)}], [M_1^{(4)}], [M_2^{(4)}]). \tag{6}$$

The total phase accumulated when the mode is rotated is obtained by summing these discrete phase contributions weighted by their multiplicities at each high-symmetry point. For the twofold-symmetric X point, this construction leads to the invariant

$$[X_1^{(2)}] = \left(n_{X,+} - n_{X,-}\right) \bmod 2,$$

which corresponds to a quantized geometric phase $\phi = \pi$, and $n_{X,+}, n_{X,-}$ are the even and odd number of modes, for a non-trivial case this should be 0. This phase reflects a parity inversion of the electromagnetic mode and remains invariant under any smooth, symmetry-preserving deformation of the system.

A similar phase-based interpretation applies at the fourfold-symmetric M point, where the rotation eigenvalues are given by $\lambda_j = e^{i\pi j/2}$ with $j = 0, 1, 2, 3$. The invariant

$$[M_1^{(4)}] = \left(n_{M,1} - n_{M,3}\right) \bmod 4,$$

measures the imbalance between conjugate rotational eigenvalues and is associated with a total accumulated phase $\phi = \pi/2$, characteristic of modes with opposite angular circulation. $n_{M,j}$ is defined as the multiplicity of eigen values, in simple words, in counts how many bands are associated with the $e^{i\pi j/2}$ phase. In contrast, the invariant

$$[M_2^{(4)}] = \left(n_{M,2} - n_{M,0}\right) \bmod 4,$$

corresponds to a phase $\phi = \pi$, linked to field configurations that change sign under a fourfold rotation. From this viewpoint, these symmetry-based invariants provide a compact and physically transparent description of the rotational phase winding of photonic modes, without invoking more elaborate topological constructs.

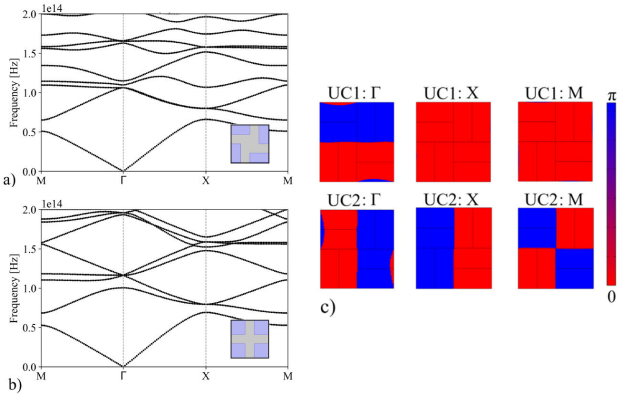


FIGURE 2. a) Band diagram for both UC1 and UC2 calculated with $a_1 = 0 = 1$, b) Shows the band diagram for the symmetric unitary call (see inset), obtained by setting $a_1 = -0.5$, according to the description in the text. c) Shows the phase diagram for each point through the Brillouin Zone of both UC1 and UC2.

In addition, through this work, the phase diagrams will serve as a tool for understanding how electromagnetic modes organize and interact within the unit cell, offering an analogy to electronic orbitals in solid-state systems.

3. Results

Once the plane is tiled, two distinct primitive cells emerge, UC1 and UC2. Both of these crystal cells generate the same 2D lattice and can be regarded as inverse representations of each other. When the side length and the lattice vector of these primitive cells are set to $a_0 = 1$ μm, both UC1 and UC2 generate the same photonic band diagram [see Fig. 2a)]. The TM mode band diagram showcases two gaps, the main one centered around 0.5×10^{14} Hz (approximately 6000 nm) and a secondary, much smaller gap at around 1.9×10^{14} Hz (about 1600 nm), as seen in Fig. 3. There is also a partial Dirac point that spans four distinct bands at a frequency around 1×10^{14} Hz.

To clarify the origin of the secondary gap relevant to the topological states, we analyze a continuous geometrical deformation of the unit cell through the parameter a_1, as shown in Fig. 2. For $a_1 = -0.5$, the silicon elements form a cross-like geometry, the unit cell symmetry is C_{4v} and its space group is $p4mm$, and the corresponding band structure exhibits the Dirac-like degeneracy associated with this higher-symmetry configuration. The parameter a_1 is introduced as a dimensionless translation factor that governs the spatial displacement of the rectangular air voids within the silicon matrix. In the finite element simulation, the position of these voids is modified by a displacement vector parameterized by a_1: $\vec{r}' = \vec{r} + a_1 L_1 \hat{u}$, where L_1 is a characteristic length of the geometry (*e.g.*, a shift along the vertical would be $\Delta y = a_1 L_1$). This acts strictly as an analytical tool to explore the geometric symmetries of the lattice. As shown in Fig. 2, setting $a_1 = -0.5$ forces the air voids to converge into a central cross-like geometry, introducing mirror symmetry and a corresponding Dirac-like degeneracy. The integer values $a_1 = 0$ and $a_1 = 1$ exactly recover the perfect corner-sharing configurations of the primitive cells UC1 and UC2, respectively. It is important to note that for intermediate fractional values (e.g., $0 < a_1 < 1$), the translation disrupts the seamless tiling of the pinwheel pattern, resulting in disjointed geometries where the squares do not perfectly fit together. Therefore, the continuous sweep of a_1 does not represent a physically realizable crystalline phase, but rather a theoretical mechanism to demonstrate how breaking the higher-symmetry configuration lifts the degeneracy and opens the relevant topological band gap between bands 8 and 9.

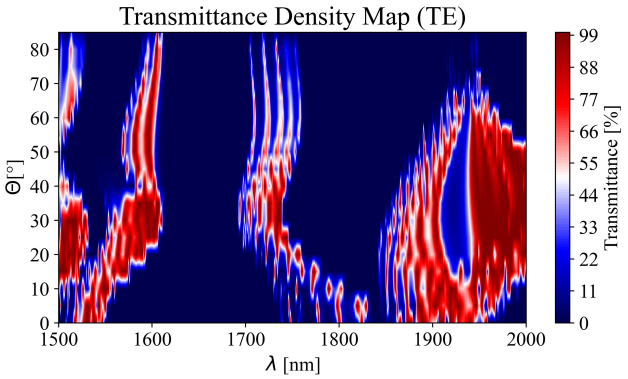


FIGURE 3. Transmittance density map showcasing the omnidirectional band gap that forms at around 1600 nm, in agreement with the band structure shown in Fig. 2.

In the periodic Bloch calculation, UC1 and UC2 describe the same underlying square lattice and yield equivalent bulk band structures, while the symmetry analysis of their eigenmodes distinguishes their topological character. The gap between bands 8 and 9 is therefore the relevant bulk gap in which the topological boundary and corner states are subsequently identified.

Phase diagrams are a useful tool for predicting not only topological phenomena but also other light-matter interactions. In this context, they serve as analogs to atomic orbitals in electronic theory. In combination with band diagrams, they provide information about how light propagates along the structure. For example, while both UC1 and UC2 generate the same band structure, propagating modes for each cell can be different for the same given k-number; they may reach the same destination, yet the way they reach it is what makes both UCs distinct.

The phase diagrams shown in Fig. 2c), reveal that both UC1 and UC2 present a p-like orbital at the Γ point, p_x for UC1 and p_y for UC2. For the other points, UC1 exhibits s orbital configurations, whereas UC2 at the X point remains as a p_x orbital. Furthermore, at the M point, it has a d_{xy}-like orbital phase configuration. This showcases evidence that, while both unitary cells produce the same band diagram, the phase analysis indicates a difference in which modes can propagate through each structure.

The band structure and symmetry analysis therefore provide a consistent picture of the two complementary primitive-cell configurations. In particular, the opening of the gap upon departing from the higher-symmetry configuration provides the bulk spectral region in which the topological properties of the corresponding bands can be analyzed.

Tables I and II showcase the topological invariants made to both UC1 and UC2. Given that our point of interest is located very high in the frequency domain, nearly at 2×10^{14} Hz, it is of great importance that we consider the topological class from all the bands below, including the one of interest.

So, from Table I we can see that although a subset of bands in UC1 (bands 3, 5, 7, and 9) display stable topological invariants, the majority of the low-lying bands yield the trivial vector $(0, 0, 0)$, which corresponds to fragile topology. This predominance of fragile indicators, together with the absence of robust non-trivial symmetry indices in most bands, supports the interpretation of UC1 as the topologically trivial unit cell. In contrast, the analysis of Table II, focused on UC2, reveals a predominance of stable indicators, with bands 1, 2, 3, 5, 6, and 10 displaying non-trivial vectors of the form

TABLE I. Symmetry vector for the first ten bands for UC1.

Band	UC1 $([X_1^{(2)}],[M_1^{(4)}],[M_2^{(4)}])$	UC1 Class.
1	$(0,0,0)$	Trivial
2	$(0,0,0)$	Trivial
3	$(+1,0,-1)$	Stable
4	$(0,0,0)$	Trivial
5	$(-1,0,+1)$	Stable
6	$(0,0,0)$	Trivial
7	$(-1,0,+1)$	Stable
8	$(0,0,0)$	Trivial
9	$(-1,0,+1)$	Stable
10	$(0,0,0)$	Trivial

TABLE II. Symmetry vector for the first ten bands for UC2.

Band	UC2 $([X_1^{(2)}],[M_1^{(4)}],[M_2^{(4)}])$	UC2 Class.
1	$(-1,0,+1)$	Stable
2	$(+1,0,-1)$	Stable
3	$(-1,0,+1)$	Stable
4	$(0,0,0)$	Trivial
5	$(-1,0,+1)$	Stable
6	$(+1,0,-1)$	Stable
7	$(0,0,0)$	Trivial
8	$(0,0,0)$	Trivial
9	$(0,0,0)$	Trivial
10	$(+1,0,-1)$	Stable

$(\pm1,0,\mp1,0)$. These configurations cannot be decomposed into non-negative combinations of atomic limits, confirming their stable topological nature. Although a few bands (4, 7, 8, and 9) exhibit fragile indicators with trivial vectors $(0,0,0)$, the overall band structure is dominated by stable topological signatures. This establishes UC2 as the non-trivial unit cell, in sharp contrast to UC1; all of this in agrement with the literature [23,24].

3.1. Topological edge states

Once the trivial and non-trivial hierarchy between UC1 and UC2 is established, we can construct the finite crystal supercell. In Fig. 4, we show the design of the combined UC1-UC2 finite photonic system, suitably combining lattices with trivial and non-trivial unit cells. The system consists of a 20×20 array of UC1 unit cells, within which a smaller 10×10 region composed of UC2 unit cells is embedded. The UC1 subregion is positioned such that its bottom-left corner is centered

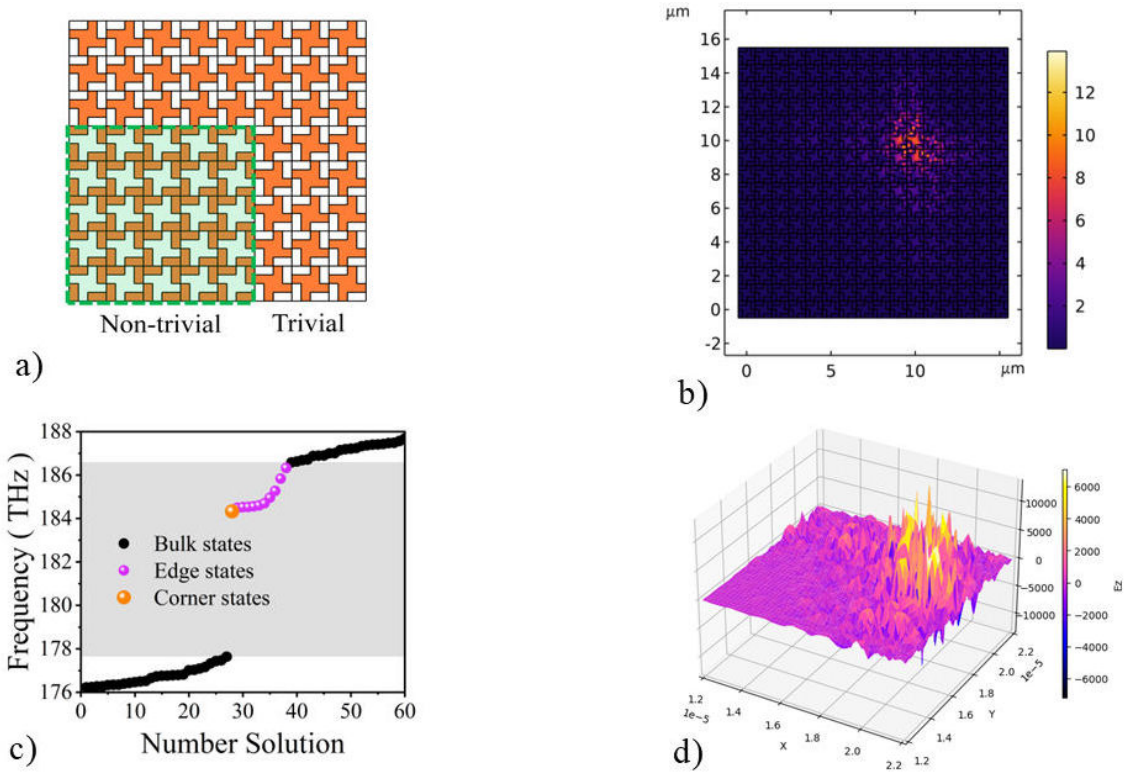


FIGURE 4. a) Representation of the finite crystal, centered around one of the corners. b) Localized edge state for the light mode of frequency 1.8471×10^{14} Hz, for the E_z component of the electric field. c) Graph for the eigen frequencies and number of solutions of our system. d) Height map for the Ez component at the edge state.

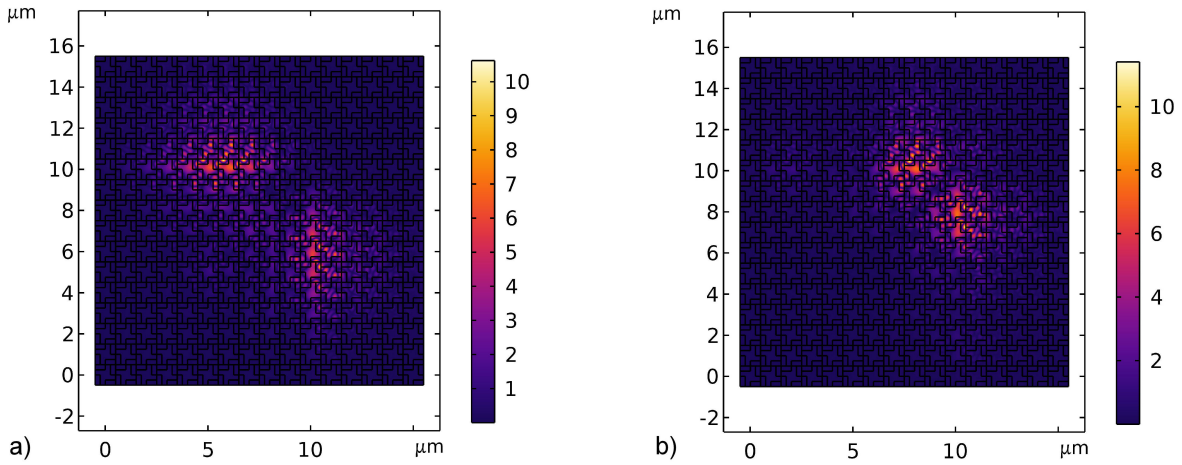


FIGURE 5. a) shows an edge that appears at a frequency of 1.8449×10^{14} Hz, and goes around the dislocation, b) a more concentrated edge state at around 1.8433×10^{14} Hz.

is centered at the coordinate origin, $(0, 0)$ [see Fig. 4a)]. We assume the incidence of a Gaussian-like light beam from the negative x-direction. It is possible to observe a localized, corner-like mode of light propagation [Fig. 4b)], corresponding to a frequency of $\sim 1.8471 \times 10^{14}$ Hz, correctly predicted by the number of solutions. Figure 4c) shows the diagram of frequency against the number of solutions, illustrating a clear bulk band gap in which localized states emerge, consistent with a nontrivial topological phase in the two-dimensional photonic crystal [22]. Bulk modes form two separated continua, while edge states appear within the gap and smoothly connect the bands, indicating topologically protected boundary propagation. Additionally, an isolated corner state is observed inside the gap, spectrally separated from the edge branch. Finally, a plot of the z-component of the electric field [Fig. 4d)] shows quite strong localization of its amplitude on both sides of the edge, although there is still some non-zero intensity away from it along the edges toward the frontier of the system. From the frequency of this mode alone, one can see that our design is highly sensitive to the frequency, in part due to its location in the band diagram, as well as the unitary cells themselves. We have also identified the presence of a well defined topological border-like state at around 1.8471×10^{14} Hz [see Fig. 5a)]. There, as well as for the aforementioned corner-like state, we are firmly within the 10th photonic band. Therefore, it was convenient to calculate the topological invariant not only for the first band but also for the lowest ten bands, as reported in Tables I and II for each of the unit cells involved. In Fig. 5, we represent additional topological states that showcase the propagation of light through the boundary. Fig. 5a) shows an edge mode that appears at a frequency of 1.8449×10^{14} Hz and goes around the dislocation; however, it does not exhibit the cardioid-like structure at the corner. In addition, Fig. 5b) shows another edge state at around 1.8433×10^{14} Hz, respectively. Unlike the main mode, which is highly localized around the corner of the embedded square, these other modes propagate around the lattice edges.

3.2. Near-zero refractive index

By observing the photonic band diagram, it is possible to note that at the Γ point, around 1×10^{14} Hz, there is a collection of bands that form a Dirac cone. Zooming into this region reveals four bands in close proximity. Two of these bands -colored orange and green, [see the lowest depicted ones in Fig. 6a)]- are particularly relevant, with a third band appearing near the Dirac point. This arrangement resembles configurations typically observed in near-zero index (NZI) phenomena. Such systems allow for unique wave propagation properties, such as uniform phase across space or enhanced tunneling, and often involve specific band structures near the Γ point that resemble Dirac-like dispersions [25,26].

One key distinction, however, lies in the orbital composition of the bands involved. While NZI systems often feature an $s - p - p$ or monopole-dipole-dipole orbital distribution, the case examined here may differ in the exact orbital character of the bands forming the Dirac cone. This difference in orbital symmetry can have important implications for both the photonic behavior and potential topological properties of the system.

In an ideal NZI crystal, the electric field must be uniform at the scale of the unit cell, with a uniform phase across the supercell and omnidirectional propagation [27-29]. From the perspectives of symmetry and photonic band theory, our orbital dipole-dipole-quadrupole ($p - p - d$) distribution fully satisfies these criteria. At the Γ point, the point group symmetry is C_4. While C_4 is an Abelian group with strictly one-dimensional irreducible representations, the double degeneracy of the p_x/p_y modes is guaranteed by time-reversal symmetry, which pairs the two complex-conjugate one-dimensional representations. And is, therefore, symmetry-protected to be degenerate, while the quadrupole mode (d_{xy}, belonging to B_1 or B_2) can naturally lie above them if the geometry or material parameters invert the conventional $s - p - p$ ordering.

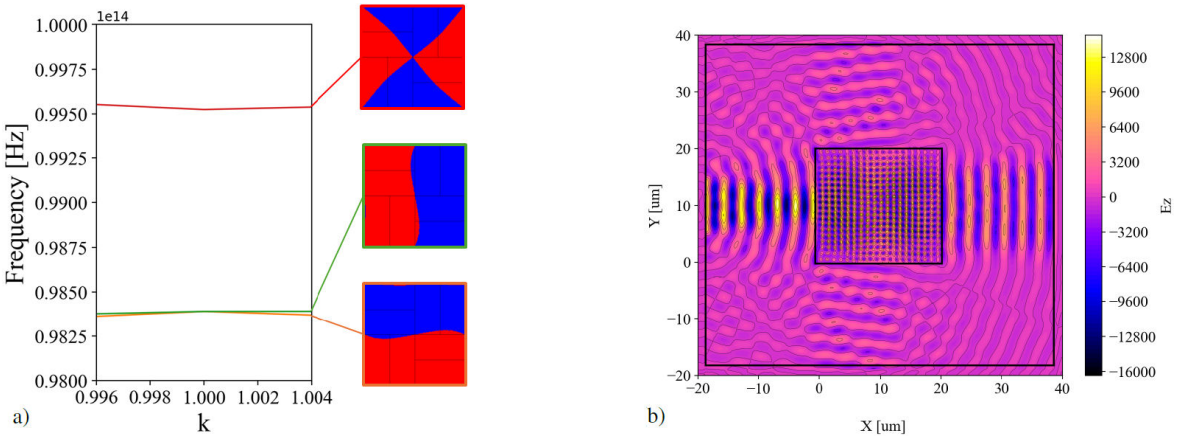


FIGURE 6. a) Band diagram of the two bands that form the Dirac point near a third upper band, the phase diagrams represent the orbitals; from up to bottom we have, d_xy, p_y and p_x orbitals. b) 20×20 supercell simulation showcasing a near-zero refractive index using a 1.031×10^{14} Hz Gaussian beam.

If we consider the effective impedance Z_{eff}, defined as

$$Z_{\text{eff}} = \sqrt{\frac{\mu_{\text{eff}}}{\varepsilon_{\text{eff}}}}, \tag{7}$$

an ideal zero-refractive-index condition for the given mode would occur when both the effective permeability and permittivity vanish simultaneously, $\mu_{\text{eff}} = \epsilon_{\text{eff}} = 0$. The resulting finite, non-zero effective impedance Z_{eff} ensures high transmittance matching the incident medium. In our system, the p_x/p_y mode degeneracy at the Γ point is symmetry-protected by the C_4 lattice and time-reversal symmetry. However, obtaining a zero-index response requires bringing these modes into spectral overlap with an additional band. Here, the quadrupole (d) band is positioned above the p-doublet, signaling a band inversion rather than the canonical triple ($s+p+p$) accidental degeneracy [13,30]. This structural configuration yields an effective near-zero-index regime characterized by a non-ideal evanescent field profile and residual internal reflections [30].

By simulating a UC1 20x20 supercell, we can achieve a near-zero refractive index using a 1.031×10^{14} Hz (2900 nm) Gaussian beam, [see Fig. 6b)]. As commented, compared to other 2D geometries [25], our finite crystal cannot be viewed as a perfect example of a near zero index case: When such a Gaussian beam is shot from the k_x direction, the electric field at the top of the crystal does not propagate parallel to the surface of the lattice; instead, it does so in a slightly tilted way, as seen in Fig. 6b). As a result, when a beam is shot from both the k_x and k_y directions, the effect of an outgoing plane wave is not as pronounced as when the beam comes from a single direction (see Fig. 7).

In short, while the linear dispersion and associated orbital configuration with p_x/p_y degeneracy at a Dirac point can drive the effective refractive index n_{eff} toward zero, it does not inherently produce a stable near-zero-index (NZI) effect. The resulting impedance is often unstable and highly direction-dependent. As established in the literature, achieving a robust, isotropic NZI condition requires a monopolar contribution, which is absent in simple Dirac cone degeneracies [30]. Considering the relation between topological protection and effective electromagnetic properties [17], despite the Dirac cone associated with the p_x/p_y band inversion is topologically allowed and protected, this absence prevents the crystal from behaving as a fully homogeneous zero-index material, leading to a regime that can be described as a near-zero-index phase that is topologically permitted but electromagnetically incomplete. This highlights a fundamental distinction between topological robustness in momentum space and the effective behavior of the medium and its properties [17,30,31].

4. Conclusions

Squared lattices are notorious for their difficulty in generating topological photonic phenomena. Through this work, we present a squared lattice that can produce both topological and near-zero index propagation using a simple star-like design made of silicon rectangular bars. Technologically speaking, our design is suitable for reproduction using well known techniques, such as RF sputtering.

As for the optical results, the design represents a case of *jack of all trades, master of none*, since the optical phenomena observed are both of perspective interest; however, the way they manifest lacks the refinement of a device specifically made for such a task. For example, the NZI effect observed at 1.031×10^{14} Hz shows a slight deviation in the perpendicular propagation of a Gaussian beam. Making this types of devices ideal for uses in cloaking both transmission and reflection [32].

The same can be expected for the propagation of topological modes. To begin with, the frequency at which the effect can be observed appears around the 10th band in the photonic dispersion relation. This already proves difficult to diagnose its presence, thus forcing the calculation of the symmetry vector for all bands below it [20,33]. Initial results showcase a clear tendency for the unit cells labeled UC2 and UC1

to behave as non-trivial and trivial, respectively. Yet, some points within this analysis present irregularities (see Tables I and II). As a result, the stability of the topological propagation is quite low. Moreover, when simulating a boundary between two unit cells, the edge state appears to be quite sensitive to the frequency of the input signal and is surrounded by multiple cases of low propagation profiles.

Nonetheless, given the presence of two different kinds of *exotic* light propagation modes-topological and near-zero index-the photonic structure under study can be considered promising. Given the simplicity of the photonic crystal design, paired with satisfactory results for both identified phenomena, we can confidently refer to this possible device as having strong potential for applications in areas such as high-sensitivity optical sensing and signal modulation. A systematic study, perhaps involving automatic learning to improve the geometry by means of rotations or re-dimensioning [34], could lead to a 'ready to apply' design oriented to topological photonics.

Acknowledgments

MEMR, MATC, HAGU and IVPQ acknowledge Mexican SECIHTI for its support through Research Grant CBF-2025-I-1058.

1. S.-Q. Wu *et al*., All-dielectric photonic crystal with unconventional higher-order topology, Photonics Research (2021), https://doi.org/10.1364/PRJ.418689
2. J. Ma *et al*., Manipulating Second Harmonic Generation in Higher-Order Topological Photonic Crystals, Annalen der Physik **533** (2021), https://doi.org/10.1002/andp.202100191
3. B. Xie *et al*., Visualization of Higher-Order Topological Insulating Phases in Two-Dimensional Dielectric Photonic Crystals., Physical review letters **122** (2018) 233903, https://doi.org/10.1103/PhysRevLett.122.233903
4. E. Y. González-Ramírez *et al*., All-optical photonic switch via the higher-order topological spin Hall effect, *Phys. Rev. Appl.* **21** (2024) 044038, https://doi.org/10.1103/PhysRevApplied.21.044038
5. J. A. Medina-Vázquez, E. Y. González-Ramírez, and J. G. Murillo-Ramírez, Corner states in photonic higher-order Dirac semimetals, *Phys. Rev. A* **107** (2023) 053511, https://doi.org/10.1103/PhysRevA.107.053511
6. F. Zangeneh-Nejad and R. Fleury, Topological Fano Resonances, *Phys. Rev. Lett.* **122** (2019) 014301, https://doi.org/10.1103/PhysRevLett.122.014301
7. Z. Wang *et al*., Higher-order Dirac semimetal in a photonic crystal, *Physical Review B* (2022), https://doi.org/10.1103/physrevb.105.l060101
8. S. G. y. García *et al*., Atomically Thin Current Pathways in Graphene through Kekulé-O Engineering, *Nano Letters* **24** (2024) 2322, https://doi.org/10.1021/acs.nanolett.3c04703
9. M. Li *et al*., Higher-order topological states in photonic kagome crystals with long-range interactions, *Nature Photonics* **14** (2020) 89, https://doi.org/10.1038/s41566-019-0561-9
10. L. Xiong *et al*., Topological Properties of a Two-Dimensional Photonic Square Lattice without C4 and Mx(y) Symmetries, ACS Photonics (2022), https://doi.org/10.1021/acsphotonics.2c00571
11. Z.-K. Lin *et al*., Anomalous quadrupole topological insulators in two-dimensional nonsymmorphic sonic crystals, *Phys. Rev. B* **102** (2020) 035105, https://doi.org/10.1103/PhysRevB.102.035105
12. S. A. Horsley and M. Woolley, Zero-refractive-index materials and topological photonics, *Nature Physics* **17** (2020) 348-355, https://doi.org/10.1038/s41567-020-01082-2
13. X. Huang *et al*., Dirac cones induced by accidental degeneracy in photonic crystals and zero-refractive-index materials., *Nature materials* **10** (2011) 582, https://doi.org/10.1038/nmat3030
14. H. Tang *et al*., Low-Loss Zero-Index Materials., *Nano letters* (2020), https://doi.org/10.1021/acs.nanolett.0c03575
15. V. Sasse, Classification of the 17 Wallpaper Groups, https://math.uchicago.edu/ may/REU2020/ REUPapers/Sasse.pdf (2020), REU Paper, University of Chicago.
16. COMSOL AB, COMSOL Multiphysics Reference Manual, COMSOL AB, Stockholm, Sweden (2023), v. 6.2.
17. B. Bradlyn *et al*., Topological quantum chemistry, *Nature* **547** (2017) 298.
18. L. Lu, J. D. Joannopoulos, and M. Soljačić, Topological photonics, *Nature Photonics* **8** (2014) 821-829, https://doi.org/10.1038/nphoton.2014.248
19. H. C. Po, A. Vishwanath, and H. Watanabe, Symmetry-based indicators of band topology in the 230 space groups, *Nat. Commun.* **8** (2017) 50.
20. S. Vaidya *et al*., Topological phases of photonic crystals under crystalline symmetries, *Phys. Rev. B* **108** (2023) 085116, https://doi.org/10.1103/PhysRevB.108.085116
21. C. Fang and L. Fu, New classes of topological crystalline insulators having surface rotation anomaly, *Sci. Adv* **5** (2019)
22. W. A. Benalcazar, T. Li, and T. L. Hughes, Quantization of fractional corner charge in C-n- symmetric higher-order topological crystalline insulators, *Physical Review B* **99** (2019), https://doi.org/10.1103/physrevb.99.245151

23. Y. Chen, J. Li, and J. Zhu, Topology optimization of quantum spin hall effect-based second-order phononic topological insulator, *Mechanical Systems and Signal Processing* **164** (2022) 108243, https://doi.org/10.1016/j.ymssp.2021.108243

24. B. Xie *et al*., Second-order photonic topological insulator with corner states, *Phys. Rev. B* **98** (2018) 205147, https://doi.org/10.1103/PhysRevB.98.205147

25. L. Vertchenko *et al*., Near-Zero Index Photonic Crystals with Directive Bound States in the Continuum, *Laser & Photonics Reviews* **15** (2021) 2000559, https://doi.org/10.1002/lpor.202000559

26. L. Vertchenko, M. Nikitin, and A. Lavrinenko, Near-zero-index platform in photonics: tutorial, *J. Opt. Soc. Am. B* **40** (2023) 1467, https://doi.org/10.1364/JOSAB.489055

27. M. W. Ashraf and M. Faryad, On the mapping of Diraclike cone dispersion in dielectric photonic crystals to an effective zero-index medium, *J. Opt. Soc. Am. B* **33** (2016) 1008, https://doi.org/10.1364/JOSAB.33.001008

28. I. Liberal and N. Engheta, Near-zero refractive index photonics, *Nature Photonics* **11** (2017) 149-158, https://doi.org/10.1038/nphoton.2017.13

29. M. Minkov *et al*., Zero-Index Bound States in the Continuum., *Physical review letters* **121** (2018) 263901, https://doi.org/10.1103/physrevlett.121.263901

30. X. Huang *et al*., Dirac cones induced by accidental degeneracy in photonic crystals and zero-refractive-index materials, *Nature Materials* **10** (2011) 582-586, https://doi.org/10.1038/nmat3030

31. G.-G. Wei *et al*., Zero refractive index properties of twodimensional photonic crystals with Dirac cones, *Chinese Physics Letters* **36** (2019) 034203, https://doi.org/10.1088/0256-307x/36/3/034203

32. T. Luo *et al*., Transmission and reflection cloaking by using a zero-refractive-index photonic crystal in the microwave region., *Applied optics* **60** (2021) 7492, https://doi.org/10.1364/ao.430234

33. M. D. de Paz *et al*., Engineering fragile topology in photonic crystals: Topological quantum chemistry of light, *Physical Review Research* (2019), https://doi.org/10.1103/physrevresearch.1.032005

34. J. G. Cardona *et al*., Flat band fine-tuning in photonic crystals via unsupervised shape artificial intelligence, *Optik* (2024) 172669.